Numerical Study of Mixing and Thermal Conduction of Granular Particles in Rotating Tumblers

Nan Gui
State Key Laboratory of Heavy Oil Processing, China University of Petroleum, Beijing, 102249 P.R. China

College of Mechanical and Transportation Engineering, China University of Petroleum, Beijing, 102249 P.R. China

Jinsen Gao
State Key Laboratory of Heavy Oil Processing, China University of Petroleum, Beijing, 102249 P.R. China

Zhongli Ji
College of Mechanical and Transportation Engineering, China University of Petroleum, Beijing, 102249 P.R. China

DOI 10.1002/aic.13999
Published online January 24, 2013 in Wiley Online Library (wileyonlinelibrary.com)

A discrete element method (DEM) study is conducted to investigate the mixing and heat-transfer characteristics of steel spherical particles under various rotation speeds and flow regimes of a rotating tumbler. The mixing degree, weighted temperature, temperature discrepancy at the mixing interface, temperature radial distribution, and information entropy are used to analyze the effect of mixing structure and evolution duration on the heat-transfer characteristics. The results under the same revolution and the same evolution time are compared to show the effects of evolution time and mixing structure on thermal conduction. After a detailed analysis, the joint contribution of mixing degree and duration to granular heat transfer is explained, and the different approaches in static thermal conduction and dynamic mixing are shown. Moreover, a new method is proposed using the mean increase rate of temperature information entropy to determine the most effective operating condition for thermal conduction in granular particles. © 2013 American Institute of Chemical Engineers *AIChE J*, 59: 1906–1918, 2013

Keywords: rotating tumbler, mixing, granular particle, thermal conduction, discrete element method, information entropy

Introduction

Rotating tumblers are currently employed by chemical industries in a wide variety of physical processes, including size reduction, waste reclamation, agglomeration, solid mixing, drying, heating, cooling, etc. The widespread use of rotating tumblers is also caused by its ability to handle various feedstocks, from slurries to granular materials, and to operate in distinct environments.[1] Thus, the mixing and heat transfer of granular materials in rotating tumblers have received substantial attention over the past few years.

For mixing of granular materials, McCarthy et al.[2] studied the avalanche mixing of granular solids in slowly rotating tumblers. Avalanche mixing is described geometrically as a mapping of avalanching wedges, i.e., transporting an initial wedge of material downhill to a new wedge. They extended the model to handle complicated geometries, including that for three-dimensional (3-D) mixer, mixing enhancement testing, incorporating different particles, etc. Similarly, Cisar et al.[3] studied the effect of tumbler shapes and fill fractions on mixing of particles based on the models of cellular automata and mapping of wedge region, respectively. Meier et al.[4] studied the complicated granular mixing in 3-D systems. Their observation led to a simple, compact, and extensible continuum-based dynamical system framework applicable for time-periodic flow in 3-D systems rotating about one or more axes of rotation.

In terms of analytical descriptions, Mellmann et al.[5] proposed mathematical models to calculate the transverse solid motion based on mass and momentum balances. McCoy et al.[6] applied a population balance approach to describe the size-distributed cluster processes and derived expressions for mixing effectiveness and segregation measures. Mellmann[7] developed mathematical models to predict the transition between different forms of transverse motion of free-flowing bed materials in rotating cylinders. These models worked out the transition criteria, which can provide the possibility of estimating the type of motion of bed materials.

As regards to numerical studies, Wightman et al.[8] used the discrete element method (DEM) to model the mixing of particles in a rotating and rocking cylinder and found a dramatic enhancement in mixing through the impartment of

Correspondence concerning this article should be addressed to J. Gao at jsgao@cup.edu.cn and N. Gui at zjuguinan@zju.edu.cn.

rocking motion on the rotating motion. Portillo et al.[9] presented a hybrid approach to model solid mixing based on the DEM as well compartment modeling with the aim of reducing computational expense. Vargas et al.[10] employed a DEM simulation to investigate the segregation suppression of granular mixtures. Geng et al.[11] studied the mixing kinetics of slender particles in a rotary dryer using the DEM. Additionally, Cleary and Sinnott[12] demonstrated how DEM can be used to unravel flow dynamics and assess mixing in several different types of devices. They also determined whether Froude number scaling is suitable for predicting the scale performance of rotating mixers.

Many experimental studies on drum dynamics were performed based on various modern and efficient methods, including visual observation of tagged particles,[13] radioactively labeled tracer particles (positron emission particle tracking, PEPT),[14] magnetic resonance imaging (MRI),[15] and image analysis programming,[16] etc. The penetrating methods of PEPT and MRI are noninvasive and can determine accurately the locations of traced particles. Thus, these methods enable the feasibility of studies on particle mixing in long rotating cylinders and actual engineering structures as well as adjusting the key parameters, such as the friction coefficient, in numerical simulations based on the best agreement between numerical and experimental results.

Based on these studies, granular mixing is unquestionably important and widely investigated in the physics and engineering communities. However, its knowledge base is still poorly understood.[17] As a result, the heat transfer between granular materials, which is closely related to the mixing process, is also poorly understood.

In relation to the solid mixing and heating processes in rotating tumblers, Kwapinska et al.[18] studied the mixing of particles in rotary drums through a comparison of DEM results with experimental results. The DEM results were also compared with the penetration/continuum models. The penetration models were found to provide only a very coarse description of mechanical mixing and significantly underestimate its intensity. Thus, they pointed out the soundness of the DEM approach as a replacement for the continuum models in thermal process modeling. Moreover, Kwapinska et al.[19] carried out a comparison of continuous and discrete modeling of heat transfer in rotary drums. By simulating the heating process of free-flowing particles in contact with the wall of the rotary drum, they elaborated on the ability of thermal DEM to provide information not accessible by the penetration model, such as temperature distributions. They also pointed out the necessity of reducing computational cost for the thermal DEM simulation.

Shi et al.[20] employed the DEM—CFD and heat-transfer calculation coupled method to simulate realistic heat transfer in a rotary kiln, tracking the transition from convection-dominated to conduction-dominated heat transfer. They presented the important role of solid-solid conduction for higher particle conductivities. Figueroa et al.[21] used thermal particle dynamics to examine the interplay between transient heat transfer and particle mixing in rotating tumblers, determining the effect of mixing and heating rates on granular materials under different tumbler shapes and operating parameters, such as rotating rate and filling level. They used the Péclet number to determine the dominant heating mechanism, i.e., conduction or convection, and to predict the conditions favoring a more rapid flow of thermal energy. The results showed that increasing the mixing rate is detrimental to bed heating because of the reduction in collision time between the bed wall and particles.

Many signal processing methods have also been used to characterize granular mixing or heat transfer, such as power spectrum analysis, fractal analysis, wavelet analysis, and information entropy analysis. Among these methods, the Shannon information entropy-based analysis should be considered. The Shannon entropy can be used to evaluate the degree of uncertainty involved in predicting the output of a probabilistic event.[22] For example, to analyze the complicated temperature fluctuating phenomenon, mutual information and the Shannon entropy were employed by Cho et al.[23] to study heat transfer in the riser of a three-phase circulating fluidized bed. Zhong and Zhang[24] employed the Shannon entropy analysis of pressure fluctuations to characterize dynamic behavior. The results showed that the Shannon entropy aids in highlighting the complex characteristics of the dynamic behavior of granular particles. Thus, this study will also employ the Shannon entropy to characterize granular mixing and conduction. Moreover, different from all previous methods based on the local information of concentration or temperature,[23,24] in this study, specific interests are focused on the macroscopic degree or global level of granular mixing and heat transfer.

A wide area for the study of the characteristics of mixing and heat transfer of granular materials, particularly for heat transfer, remains. Thus, although there have pioneering works on the mixing and heating processes in rotating tumblers as reviewed earlier, the characteristics of the mixing interface and the effects of the microscopic mixing degree and macroscopic mixing level on heat transfer of granular materials are still not clearly understood. In particular, the criteria for choosing the most effective rotating tumbler under a given energy input are still unclear.

Thus, this study is conducted to investigate the intrinsic characteristics of particle mixing and thermal conduction characteristics in rotating tumblers, especially the effect of macroscopic and microscopic mixing structures on heat transfer.

Numerical Models

Particle–particle collision model

In this study, a quasi-2-D rotating tumbler (with only one layer of spheres) is simulated. The granular system is composed of steel particles belonging to the dense particulate flow regime. Thus, particle–particle collision is simulated in a deterministic way through DEM, which is a soft-sphere approach, because of its advantage in multiple-body contact dynamics.[25] The key feature of the soft-sphere approach is that three fundamental interparticle collision mechanisms, namely, elastic collision, viscous damping process, and friction or sliding trend effect, are considered to model the particle–particle interactions. Thus, the contact force of any individual particle is formulated as

$$\boldsymbol{f}_c = -k\boldsymbol{x} - \beta\dot{\boldsymbol{x}}. \qquad \text{if } |\boldsymbol{f}_c \bullet \boldsymbol{t}| > \gamma|\boldsymbol{f}_c \bullet \boldsymbol{n}|, \text{then } |\boldsymbol{f}_c \bullet \boldsymbol{t}| = \gamma|\boldsymbol{f}_c \bullet \boldsymbol{n}|, \quad (1)$$

where $\boldsymbol{f}_c$ and $\boldsymbol{x}$ are the contact force and inter-particle displacement, respectively. "•" denotes the time derivative. k and β are the collision stiffness and coefficient of damping, respectively. $\boldsymbol{t}$ and $\boldsymbol{n}$ denote the tangential and normal directions between a pair of colliding particles, respectively. It is

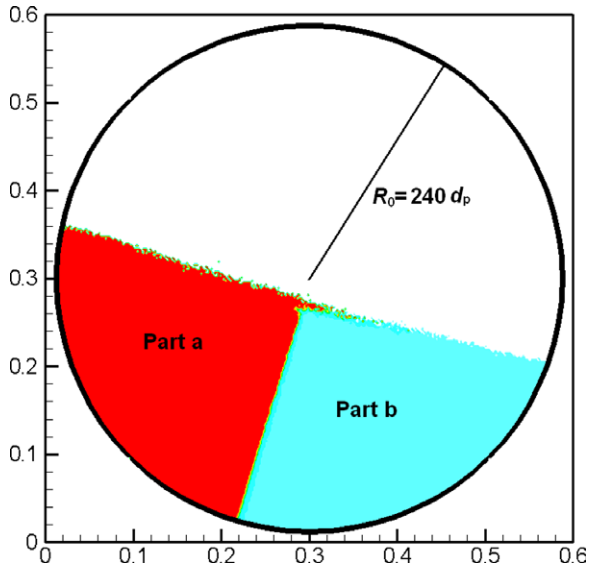

Figure 1. Sketch of the simulation setup.

[Color figure can be viewed in the online issue, which is available at wileyonlinelibrary.com.]

noticed that Eq. 1 is a vector equation, including the expressions in both the normal and tangential directions. If interparticle sliding occurs, i.e. if $|\boldsymbol{f}_c \cdot \boldsymbol{t}| > \gamma |\boldsymbol{f}_c \cdot \boldsymbol{n}|$, the tangential contact force is calculated by the friction law $|\boldsymbol{f}_c \cdot \boldsymbol{t}| = \gamma |\boldsymbol{f}_c \cdot \boldsymbol{n}|$.

Following Newton's law of motion, the translational and rotational motions of any particle are obtained by integrating the following equations

$$\ddot{\boldsymbol{x}} = \frac{\boldsymbol{F}}{m_p}, \tag{2}$$

$$\dot{\omega}_p = \boldsymbol{T}_p / I_p, \tag{3}$$

where $\boldsymbol{F} = \sum \boldsymbol{f}_c + \mathbf{g}$, is the total force experienced by any individual particle, m_p, $\boldsymbol{T}_p$, and I_p are the mass, torque, and moment of inertia of the particle, respectively, and $\boldsymbol{g}$ is the acceleration due to gravity.

Initially, the tumbler is partially filled with spherical granular particles that settle at the bottom. For the boundary condition, the tumbler is considered a rigid, motion-controlled large particle with finite radius, infinite mass and frictional adiabatic walls. Then, the tumbler is rotated with gradually increasing rotating angular velocity until it reaches a target speed (the rotating acceleration is $\dot{\omega} = \pi \text{rad}/\text{s}^2$). Six typical rotation speeds are simulated, ranging from $\omega = 0.5\pi$ rad/s to $\omega = 3.0\pi$ rad/s. A sufficiently fine time step of $dt = 5$ μs is used to stabilize the particle–particle collision simulation.

For clarity, the geometry of the tumbler is shown in Figure 1. The particles are divided into Part "a" with high temperature, and Part "b" with low temperature. The tumbler boundary is adiabatic and rotates clockwise. The parameters used in the simulation are listed in Table 1.

Particle–particle heat-transfer model

In the tumbler, several heat-transfer processes may exist, including thermal conduction among particle–particle, interstitial gas-particle, etc.; convection of fluids; and radiation heat transfer among others.[26] As long as the fluid phase is air, the ratio of conductivity for this work is $\lambda_p/\lambda_f > 2000$, where λ_p and λ_f are the thermal conductivities of the particle and air phases, respectively. Under this condition, the particle–particle conduction mechanism is expected to dominate because the ratio of conductivity of steel particles to interstitial gas is sufficiently high.[27]

Approximate analytical models of thermal conduction between two smooth, elastic particles with a finite small contact area are proposed[27] to predict the conductance from one particle centerline to the other, i.e.

$$\dot{q}_c = 2\lambda_p r_c, \tag{4}$$

where $\dot{q}_c$ is the amount of heat transported per unit temperature difference per unit time, and r_c is the contact radius. Thus, by incorporating the contact conductance concept using Eq. 4, the total amount of heat transported from the jth particle to the ith particle across their contact area per unit time is

$$\dot{Q}_{ij} = \dot{q}_c (T_j - T_i), \tag{5}$$

where T_i and T_j are their respective temperatures. Temperature variation of particle "i" is governed by

$$\frac{dT_i}{dt} = \frac{1}{c_p m_p} \sum_j \dot{Q}_{ij} \tag{6}$$

where c_p is the particle specific heat. The distribution and difference in temperature within the particle volume are neglected in Eq. 6. This condition is reasonable when the resistance to heat transfer inside the particle is considerably smaller than that among the particles,[28] i.e.

$$Bi = \frac{\dot{q}_c}{\lambda_p A_p / r_p} = \frac{2}{\pi} \frac{r_c}{r_p} \ll 1. \tag{7}$$

In this work, a very large stiffness factor is used ($K_n = 10^4$) to approximate the property of steel materials. When the particle–particle collision force is of the same order of gravity force, namely $K_n x \sim m_p g$, the ratio of interdisplacement δ_x between the pair of colliding particles to the particle diameter, i.e., $\frac{x}{d_p}$, is only about 7×10^{-10}, and $Bi \approx 3.4 \times 10^{-5} \ll 1$. Thus, the assumption of an always uniform temperature distribution within the volume of any particle is appropriate. Therefore, the thermal conduction process inside the particle volume is neglected, i.e., a quick thermal response or relaxation process inside the particle volume always dominates.

Table 1. Parameters Used in the Tumbler

Radius of gyration, R_0 (mm)	288
Number of particles, (N_a, N_b)	(45177, 45424)
Initial temperate of particles, (T_a, T_b) (°C)	(100,20)
Particle diameter, d_p (mm)	1.2
Particle density, ρ_p (kg/m^3)	7800
Particle Specific heat, C_p ($J/(kg \cdot K)$)	460
Particle Thermal conductivity, λ_p ($W/(m \cdot K)$)	46.52
Restitution coefficient, e	0.95
Friction coefficient, γ	0.3
Collision stiffness, k_n (N/m)	10000
Rotating velocity, ω/π (rad/s)	0.5, 1.0, 1.5, 2.0, 2.5, 3.0
Simulation time step, Δt (s)	5.0×10^{-6}
Total simulated time, TI (s)	25

Notes: The restitution, friction coefficients and collision stiffness are respectively the same for both particle-particle and particle-tumbler collisions.

Verification of the Numerical Models

The DEM-based model with particle–particle heat transfer was utilized and validated in a previous work by Vargas and McCarthy.[28] However, to verify this code of numerical predictions, we carried out an additional simulation with conditions similar to those of the experiment by Vargas and McCarthy. That is (1) a granular bed is packed hexagonally (Figure 2a) with 200 × 100 particles of 304 stainless steel (ρ_p=7930 kg/m^3; C_p=502 J/(kg·K); λ_p=12.1 W/(m·K)), (2) the bed is heated uniformly at the bottom and insulated at other sides, and (3) finally, a load of 5 kg is added on the bed.[28]

Therefore, no freely adjustable parameters were used in the model. However, the particles are packed in a perfect hexagonal lattice here whereas it cannot occur exactly in experiment. Thus, the stress chains might be slightly different from the experiment, and the stress inhomogeneity was not considered.

The simulated results (Figure 2b) show that (1) the numerical results are smoother and more ideal than the experimental results because of the perfectly hexagonal packing of the particles, (2) With the exception of the results of 10 min, the simulated results agree very well with the experimental results, although slight differences between them still exist, and (3) The difference of 10 min may have resulted from the difference in stress chains and stress inhomogeneities in the experiment. That is, the "fault" of the stress chains in the experiment may have led to the slower response of thermal conduction especially at the early stage.

It is necessary to mention that this study is for a dynamical rotating tumbler with short particle–particle contact time. Thus, the agreement at short time is more useful for validation. According to Eqs. 4–6, it is clear that the dynamical characteristics, namely temperature derivatives, are mainly determined by the thermal diffusivity, i.e., $\frac{dT_i}{dt} \sim \frac{\lambda_p}{c_p \rho_p} = \alpha$ where α is the thermal diffusivity. In this verification case $\alpha = 3.04 \times 10^{-6}$ m^2/s, and in the main simulation, $\alpha = 1.30 \times 10^{-5}$ m^2/s (Table 1), about one-order of magnitude larger than the former. Thus, to reach the same order of dynamical variation of temperature, the simulation time of 25 s (Table 1) correspond to about 4 min (about one-order of magnitude larger than 25 s) in this verification case, which is close to and under the same order of 10 min. Thus, supposing the differences for 10 min is acceptable as explained previously, the main simulation results should be reliable then.

In conclusion, this simulation codes are verified by the comparison of the numerical and experimental results.

Definitions for Analysis

Evaluation functions for mixing and heat transfer

From the macroscopic viewpoint of heat-transfer evaluation, the particles were preliminarily divided into two separate and equal parts by a vertical borderline. The left part is in red (denoted by the subscript "a") with an initial temperature of $T_a^0 = 100$°C, and the right part is in blue/green (denoted by the subscript "b") with an initial temperature of $T_b^0 = 20$°C. Mixing and heat transfer between the two parts of the particles in the tumbler occurred when it rotated. To evaluate the degree of mixing and heat transfer, evaluation functions based on the local differences in particle number concentration (n_a-n_b), and the weighted average temperature of the red and blue/green parts of the particles were used in this study.

Moreover, in the mixing evaluation, the difference in particle number concentration is normalized by the local concentration of the mixture

$$\Re(n_a, n_b) = \begin{cases} \dfrac{n_a(\mathbf{r}) - n_b(\mathbf{r})}{n_a(\mathbf{r}) + n_b(\mathbf{r})}, & \text{when } n_a(\mathbf{r}) > 0 \text{ or } \mathrm{n}_b(\mathbf{r}) > 0 \\ 0 & \text{when } \mathrm{n}_a(\mathbf{r}) = 0 \text{ and } n_b(\mathbf{r}) = 0 \end{cases}, \tag{8}$$

where $n(\mathbf{r})$ is the local number concentration of particles in $\mathbf{r}$. In the region solely occupied by the red or blue particles, i.e., the two completely separated particle parts, $\Re = 1$ or $\Re = -1$. In the well-mixed region $\Re \approx 0$.

In the heat-transfer evaluation, the concentration weighted temperature (WT) is

$$\Theta(T_a, T_b; n_a, n_b) = \begin{cases} \dfrac{1}{n_a(\mathbf{r}) + n_b(\mathbf{r})} \left(\displaystyle\sum_{j=1}^{n_a} T_{a,j} + \sum_{j=1}^{n_b} T_{b,j} \right), & \text{when } n_a + n_b > 0 \\ 0, & \text{when } n_a = n_b = 0 \end{cases}, \tag{9}$$

where $T_{a,j}$ ($\mathbf{r}$) is the temperature of the jth particle. $\Theta(T_a, T_b; n_a, n_b)$ contains four independent variables, and it does not depend solely on the thermal conduction characteristics, as both mixing and conduction can cause variation of $\Theta(T_a, T_b; n_a, n_b)$. Eliminating the mixing effect on $\Theta(T_a, T_b; n_a, n_b)$ requires the evaluation of the degree of discrepancy of $\Theta(T_a, T_b; n_a, n_b)$ from $\Theta\left(T_a^0, T_b^0; n_a, n_b\right)$ or the so-called temperature discrepancy function (TDF) $\Pi\left(T_a, T_b; T_a^0, T_b^0; n_a, n_b\right)$, where the superscript "0" denotes the initial variables at $t = 0$

$$\Pi = \begin{cases} \dfrac{1}{n_a + n_b} \left(n_a T_a^0 - \displaystyle\sum_{j=1}^{n_a} T_{a,j} + \sum_{j=1}^{n_b} T_{b,j} - n_b T_b^0 \right), & \text{when } n_a + n_b > 0 \\ 0, & \text{when } n_a = n_b = 0 \end{cases} \tag{10}$$

The derivation of Eq. 10 can be explained as follows. (1) Consider the ideal case with granular mixing only; i.e., the particles are adiabatic, and particle–particle heat conduction does not occur. The weighted local difference of temperature is

$$\Theta\left(T_a^0, T_b^0\right) = \frac{1}{n_a + n_b} \left(n_a T_{a,j}^0 - n_b T_{b,j}^0 \right), \tag{11a}$$

indicating that the difference in particle temperature is purely caused by particle mixing (2). Then, consider the practical case with heat conduction. The concentration weighted local temperature difference is

$$\Theta(T_a, T_b) = \frac{1}{n_a + n_b} \left(\sum_{j=1}^{n_a} T_{a,j} - \sum_{j=1}^{n_b} T_{b,j} \right), \tag{11b}$$

indicating that the difference in particle temperature is caused by both mixing and conduction (3). Subtract Eq. 11b from Eq. 11a to obtain Eq. 10. Taking type "a" for example, a difference can be found between Eqs. 11a and b. It is clear that $n_a T_{a,j}^0 = \sum_{j=1}^{n_a} T_{a,j}^0$ and $n_a T_{a,j}^0 - \sum_{j=1}^{n_a} T_{a,j} = \sum_{j=1}^{n_a} \left(T_{a,j}^0 - T_{a,j} \right)$. The $\left[\sum_{j=1}^{n_a} \left(T_{a,j}^0 - T_{a,j} \right) \right] / (n_a + n_b)$ infers the weighted local total temperature difference in the "a"-type particle between the cases of pure mixing $\frac{1}{n_a + n_b} \sum_{j=1}^{n_a} T_{a,j}^0 \left(\equiv \frac{n_a T_a^0}{n_a + n_b} \right.$, adiabatic

condition without thermal conduction, constant temperature), and time-varied temperature $\frac{1}{n_a+n_b}\sum_{j=1}^{n_a} T_{a,j}(t)$ (caused by both mixing and thermal conduction). Thus, the TDF can be explained as a type of quantification of temperature difference purely caused by the effect of particle–particle heat conduction.

Radial distribution function and Shannon entropy

For convenience in the analysis of mixing and heat transfer from the macroscopic perspective, the radial distribution function (RDF) is used in this study. The RDF is defined as

$$f_{ab}(r)=\frac{1}{\Omega_a}\int_{\Omega_a}\frac{1}{\Omega_b}\int_{\Omega_b}|\boldsymbol{x}_a-\boldsymbol{x}_b||_{|\boldsymbol{x}_a-\boldsymbol{x}_b|=r}d\boldsymbol{x}_a d\boldsymbol{x}_b, \quad (12)$$

where Ω_a and Ω_b are the area of the regions occupied by the "a" or "b" particles, respectively. $r=|\boldsymbol{x}_a-\boldsymbol{x}_b|$ represents the radial distance between the "a" particle at $\boldsymbol{x}_a$ and the "b" particle at $\boldsymbol{x}_b$. Thus, Eq. 12 indicates the average distance for all "b" particles to any of the "a" particles. In other words, RDF refers to the average probability of finding a "b" particle with a distance r from any given "a" particle. Moreover, $f_{ab}(r)$ is designated as the RDF.

The radial distribution of temperature can be evaluated in a similar manner, which is the so-called temperature RDF (T-RDF) $g_{ab}(r)$

$$g_{ab}(r)=\frac{1}{\Omega_a}\int_{\Omega_a}\frac{1}{\Omega_b}\int_{\Omega_b}[T_a(\boldsymbol{x}_a)-T_b(\boldsymbol{x}_b)]_{|\boldsymbol{x}_a-\boldsymbol{x}_b|=r}d\boldsymbol{x}_a d\boldsymbol{x}_b. \quad (13)$$

Assuming that the temperature field within the tumbler is homogeneous after sufficient development of the thermal conduction, T-RDF in all "r" ranges must be zero. In contrast, nonzero T-RDF may indicate the macroscopic discrepancy of temperature between the red (hot) and green (cool) particles.

Using radial distribution, the Shannon information entropy for mixing can be naturally calculated to evaluate the global level of mixing. As RDF takes into account the concept of probability of finding a particle at a distance r, substituting the RDF for the general probability function and integrating it over all the ranges of r, the Shannon entropy[29] is appropriately defined similarly as

$$S_M=-\int f_{ab}(r)\log_2 f_{ab}(r)dr. \quad (14)$$

The Shannon information unit is decibel. The information entropy must have larger values because of the many uncertainties in the radial distribution of particles in the system, i.e., a more developed state of mixing. Similarly, with respect to the global heat-transfer state, the Shannon information entropy for conduction is defined as

$$S_T=-\int g_{ab}(r)\log_2 f_{ab}(r)dr. \quad (15)$$

The state in which the discrepancy of temperature in the radial direction exists may indicate a global level of heat transfer. As g_{ab} and f_{ab} indicate the information of temperature and concentration at a radial distance r, the integral of them by Eq. 15 may indicate a macroscopic-level evaluation of the degree of heat transfer. In contrast to S_M, a large value of S_T indicates a low level of heat transfer between the hot and cool particles, whereas a small value of S_T indicates the reverse.

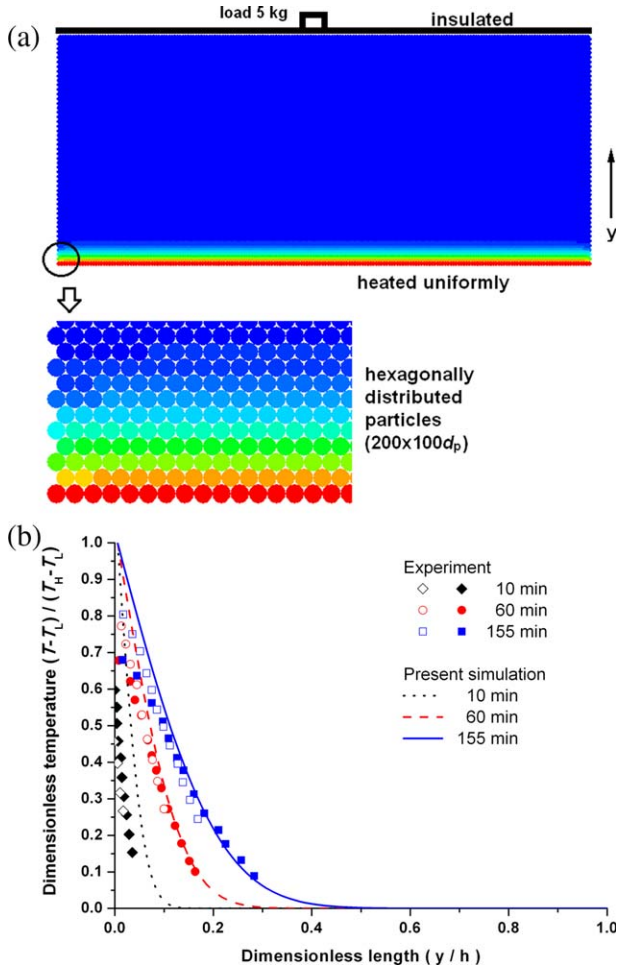

Figure 2. Additional simulation setup for simulation verification (a), and comparison between numerical and experimental results (b).

[Color figure can be viewed in the online issue, which is available at wileyonlinelibrary.com.]

In many previous studies in which information entropy was also used as a mixing parameter, entropy was always based on the local information of the concentration of particles.[29] However, this study focuses on the macroscopic perspective of the overall level of mixing degree; thus, it is based on RDF. The advantage of RDF is that it is related not only to the local information on the concentration of particles, but also to the information on the concentration of particles within a long range of distances.

Simulation Results and Discussions

Snapshots of mixing and conduction states

After the Same Evolution Time. This work investigates the results at the same evolution time and those after the same tumbler revolution to show the mixing and thermal conduction characteristics, as the amount of thermal conduction is dependent on the duration of the particle–particle contact and the degree of mixing in the tumbler.

Figure 3 shows the comparisons of the typical particle mixing state, the distribution of WT $\Re(n_a,n_b)$, and TDF $\Pi(T_a,T_b;T_a^0,T_b^0)$ at $t=8.25$ s for $\omega=0.5$ (π/s) and $\omega=1.5$ (π/s).

In the mixing and conduction process (Figure 3a and b) (1) the granular particles enter the flowing layer on the

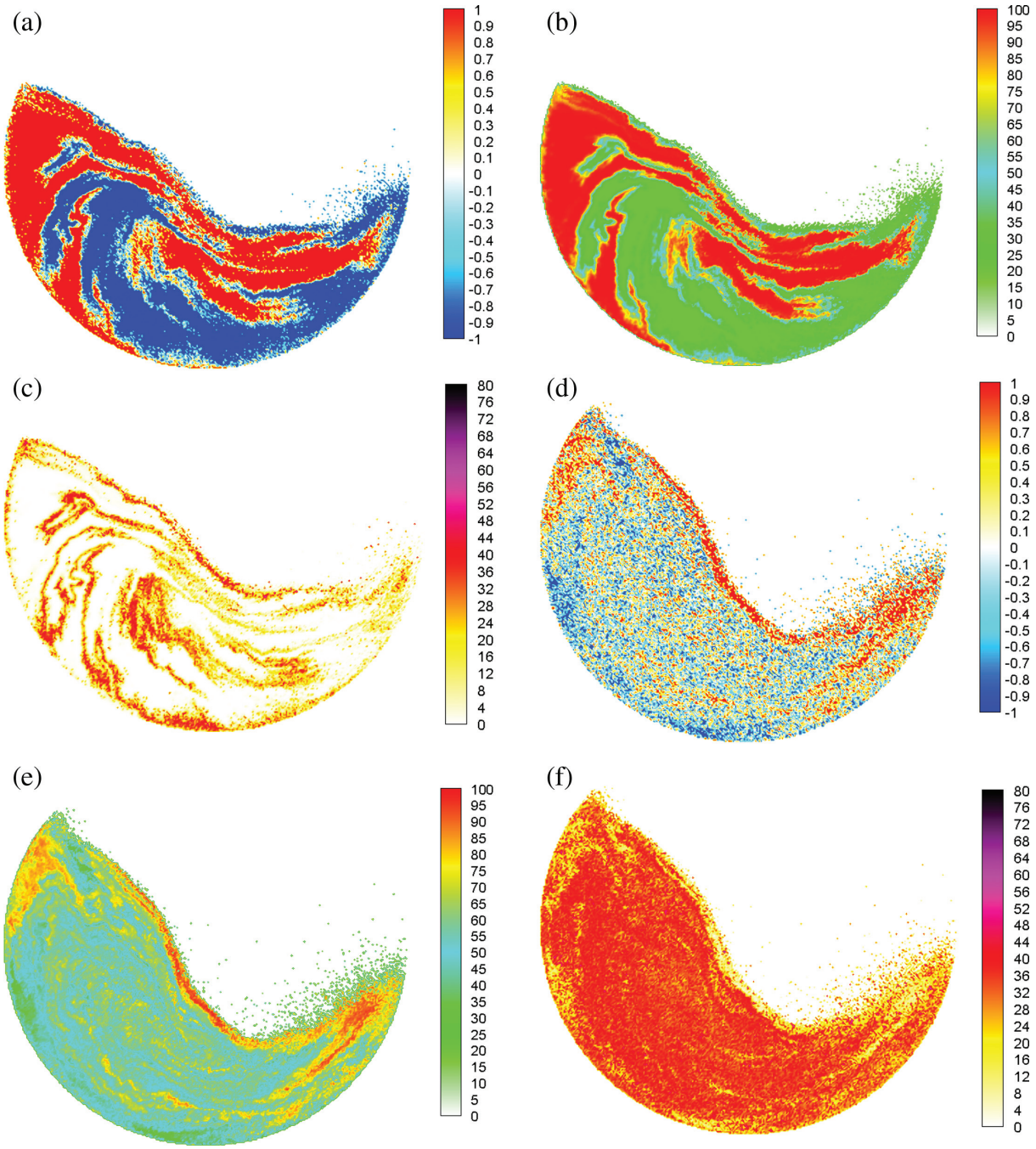

Figure 3. Comparison of mixing state $\Re(n_a, n_b)$ (*a*, *d*), WT distribution $\Theta(T_a, T_b; n_a, n_b)$ (*b*, *e*) and TDF $\Pi(T_a, T_b; T_a^0, T_b^0)$ (*c*, *f*) at t=8.25 *s* for ω=0.5(π/s) (*a*, *b*, *c*) and ω=1.5(π/s) (*d*, *e*, *f*), respectively.

left-top side, (2) they move downhill to the right-bottom side, becoming stretched, (3) they enter the static base, folded into jagged patterns, and (4) they are driven by the rotary static base with a gradual change in orientation and a slight deformation in mixing interface until they reach the left-top side again. When this process is repeated, the mixing and heat-transfer interfaces develop into increasingly finer structures (Figure 3e and f).

Comparing Figure 3a and b, after 8.25 s with only two tumbler revolutions for ω=0.5 (π/s), the mixing contour appears to be in perfect accordance with the WT distribution contour. Consistency of the mixing/conduction interfaces between the hot (red) and cool (green) particles exists not only in the fine-scale structures and large-scale skeletons of the interfaces, but also in the perfectly separated two-color contours. Moreover, TDF $\Pi(T_a, T_b; T_a^0, T_b^0)$ (Figure 3c) shows nonzero values only around the mixing interface, indicating the close dependence of conduction interface on the mixing interface.

In contrast, for ω=1.5 (π/s) after 5.63 revolutions (Figure 3d–f) with the same time of t=8.25 s, the WT distribution is composed of multiple color contours, with the TDF contours having large values in almost the entire tumbler, showing a sufficiently developed thermal conduction between the hot and cool particles after several revolutions. The mixing and conduction interface structures still agree with each other.

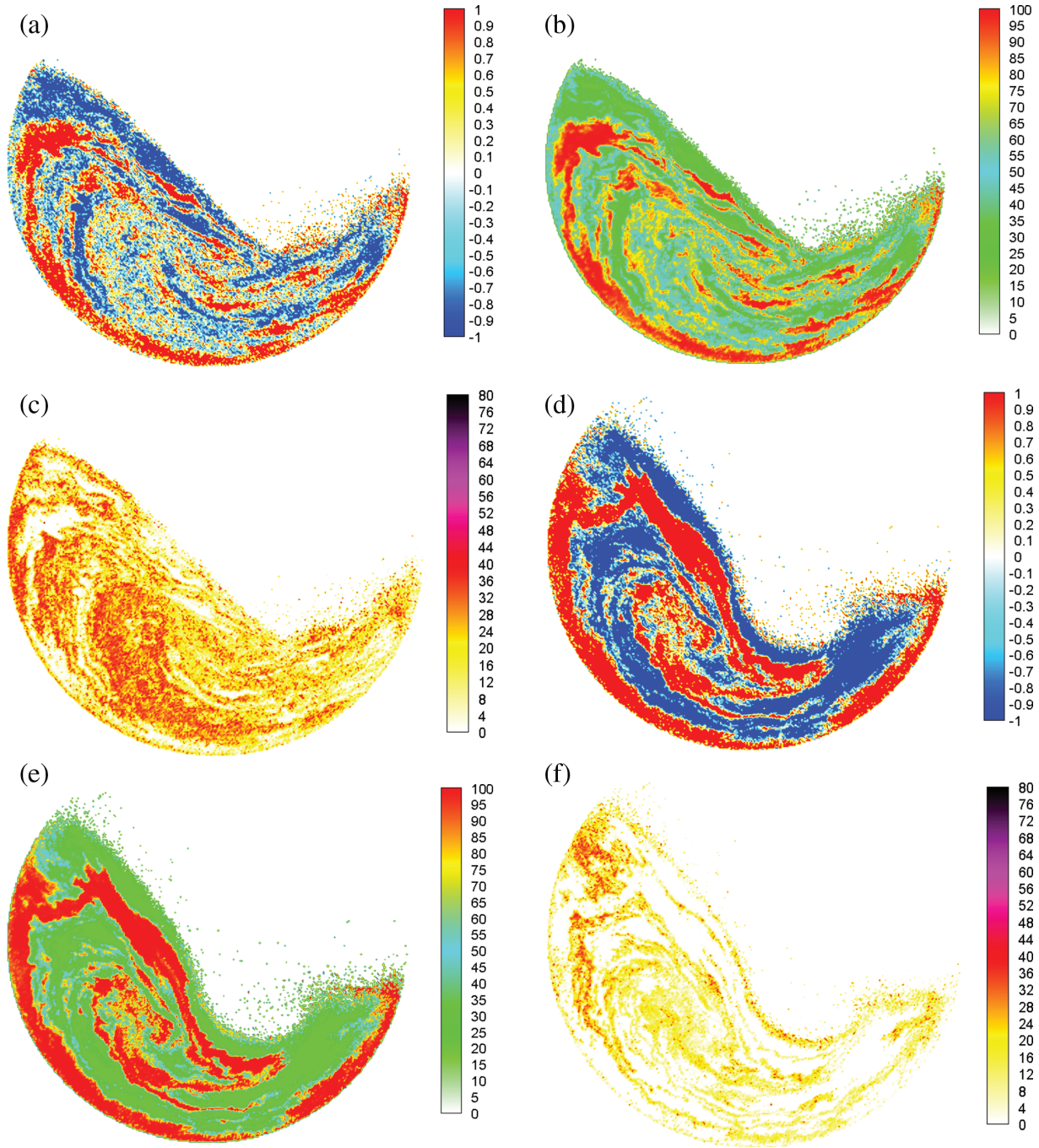

Figure 4. Comparison of mixing state $\Re(n_a, n_b)$ (*a*, *d*), WT distribution $\Theta(T_a, T_b; n_a, n_b)$ (*b*, *e*) and TDF $\Pi(T_a, T_b; T_a^0, T_b^0)$ (*c*, *f*) at two revolutions for ω=1 (π/s) (*a*, *b*, *c*) and ω=2(π/s) (*d*, *e*, *f*), respectively.

The agreement between mixing and WT contour and the comparison of TDFs in Figure 3c and f indicate the significant effect of mixing on the particle–particle heat transfer under the same temporal evolution.

After the same revolution

Figure 4 shows the comparison of snapshots of mixing and thermal conduction after two revolutions for $\omega=1$ (π/s) and $\omega=2$ (π/s), respectively. The mixing state for low-revolution speed (Figure 4a) appears slightly more developed than that for the high speed (Figure 4d) because the red and blue parts of the particles are more slender in Figure 4a than those in Figure 4d, and the structure of the mixing interface is composed of finer striations. The WT contour shown in Figure 4b has many finer striations and more light-blue/yellow-colored regions, corresponding to intermediate temperatures, than that in Figure 4e. The TDF contours (Figure 4c and f) confirm the results of Figure 4b and e of a more developed particle–particle thermal conduction at $\omega=1$ (π/s) than at $\omega=2$ (π/s).

Observing that the same revolution at low speed requires more time than that at high speed when the degrees of mixing do not differ much, the results indicate that duration and mixing degree have common effects, especially the role of duration, on the particle–particle heat transfer in the tumbler.

Mixing dimensions

Figures 3 and 4 show that the mixing structure has many hierarchical striations. This section analyzes the mixing dimension interface based on the fractal characteristics observed earlier.[30]

At the fractal interface, the length of the curve $R(s)$ is proportional to s^{-D_β}

$$R(s) \propto s^{-D_\beta}, \tag{16}$$

where D_β is the fractal dimension of the interface, and $D_\beta = -\frac{d\log R(s)}{d\log s}$, in which the Napierian base for the logarithm operation is used. Based on Eq. 16, the fractal dimension of the interface $(|\Re(n_a, n_b)| < 1, \Re(n_a, n_b) \neq 0)$ was calculated using the box-counting method.[30]

Figure 5a and b show the fractal dimension analysis of the cases corresponding to the sections entitled "After the same evolution time" and "After the same revolution", respectively. In Figure 5a, the fractal dimension for ω=0.5 (π/s) in the rolling regime is approximately D_β=1.43, and for ω=1.5 (π/s) in the rolling/cascading regime, D_β=1.87. Thus, after the same temporal rotation evolution, the low-speed rotary tumbler has a relatively less developed mixing interface than the high-speed tumbler. Less developed mixing produces more insufficient thermal conduction than does developed mixing. Thus, thermal conduction is closely related to the mixing evolution. In addition, the slight decrease in fractal dimension, i.e., mixing degree, in the very large rotation speeds of ω=2.5 and 3 (π/s) is caused by the transition from the rolling/cascading regime to the cataracting flow regime.

Subsequently, under the same number of revolutions (Figure 5b), the low-speed rotary tumbler has D_β=1.87 for ω=1.0 (π/s), whereas the high-speed rotary tumbler has D_β=1.46 for ω=2.0 (π/s). More importantly, although the fractal dimensions are different, the log(R) for different revolution speeds remains almost the same when log(s)=−4.4, corresponding to large-scale structures (log(s)=−4.4 for s=10.23 d_p, and log(s)=−5.6 for s=3.08 d_p, d_p =1.2 × 10^{-3} m, see Table 1). Thus, the differences in the relationship between log(R) and log (s) shown in Figures 5a and b are not qualitatively the same. In other words, the log(R)–log (s) relationship between ω=0.5 (π/s) and ω=1.5 (π/s) shown in Figure 5a differs from each other both in the large and small mixing scales. In contrast, the log(R)–log (s) relationship between ω=1 (π/s) and ω=2 (π/s) shown in Figure 5b differs only in small mixing scales, whereas it is the same in large-scale structures.

Recalling to the typical mixing process as mentioned previously (see section "After the same evolution time"), and referring to the basic observations of mixing patterns by Metcalfe et al.[17], the underlying mechanisms for the aforementioned differences can be explained as follows: (1) Mixing can be divided into two distinct parts, transport of so-called wedges (namely blocks of particles) and transport within wedges; (2) although differing in rotation speeds which influence the transport procedures much, the basic mechanisms of these two types of transport may remain; (3) it is reasonable to assume that the transport-of-wedge (TOW) procedure is mainly determined by the number of revolutions, and the transport-within-wedge (TWW) procedure is mainly determined by the specific mixing dynamics in the flowing layer, i.e., the downhill motion of each particle from the left-top side to the right-low side during each TOW procedure. Notice that the TWW procedure is an accompanying procedure of TOW. It is mainly determined by the numbers of TOW but needs more sufficient time to accomplish, i.e.

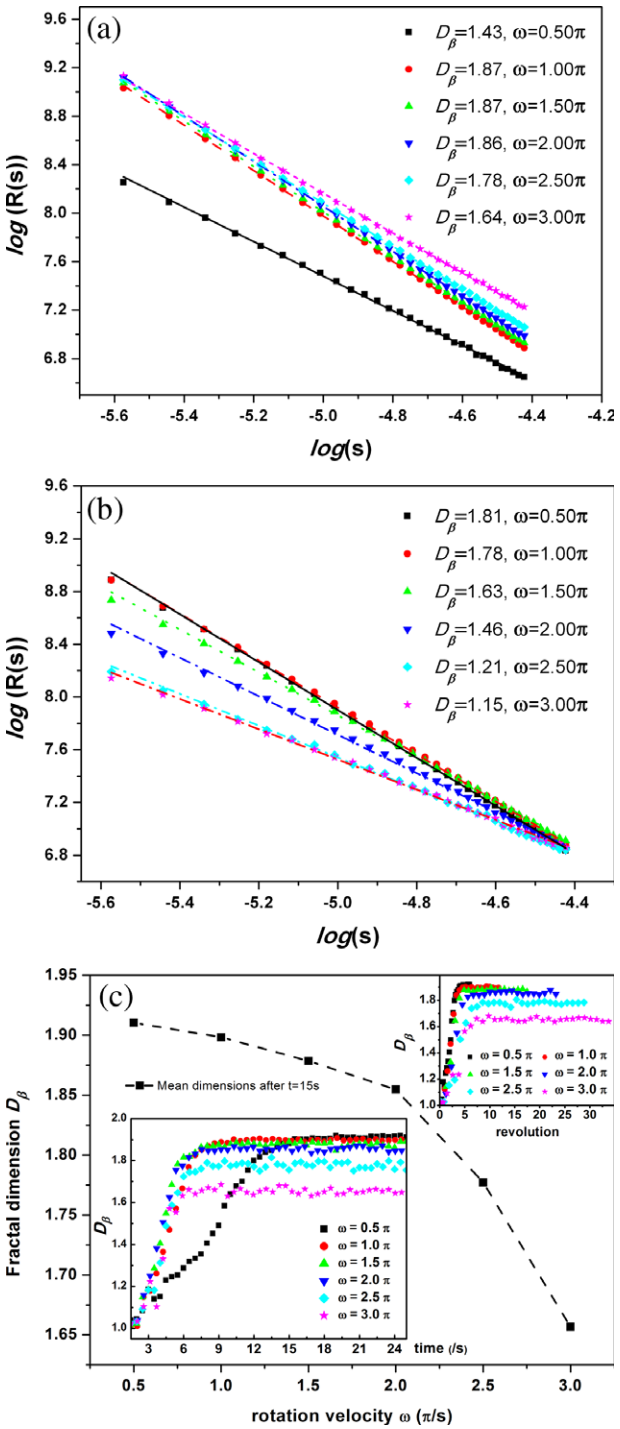

Figure 5. Relationship between the log(R)-log(s) (scatters) and their linear regressions (lines) corresponding to Figure 3 (5a) and Figure 4 (5b), respectively, and the mean developed mixing dimensions (after t=15 s) at different rotation speeds (5 c), and the evolutions of them (the insets of Figure 5c).

[Color figure can be viewed in the online issue, which is available at wileyonlinelibrary.com.]

TWW=TWW (TOW, Δt), and (4) it is also reasonable to consider that the TOW procedure determines mainly the large structures of mixing interface (interface between large blocks), whereas the TWW procedure determines mainly the fine structures (interface between fine particles).

Based on the aforementioned analysis, for this simulation, TWW procedure may have insufficient time to accomplish under larger rotation particles, whereas TOW procedure should take place at least once per revolution. Thus, under the same evolution time, a larger rotation speed produces a larger number of revolutions. The TOW makes larger contributions to the large-scale mixing interface then. Meanwhile, the TWW contribution is increased as the number of TOW increases although the evolution time is the same. Thus, both the large and small scales of mixing interface are increased as the rotation speed increases. In contrast, under the same number of revolutions, the TOW contribution remains the same. The TWW contribution is determined by the duration time then. As a result, a smaller rotation speed leads to more small-scale interface as it needs more time to reach the same revolution.

Thus, the difference in the mixing degree under the same revolution is not as evident as before, and it appears to be the same from the large-scale point of view. However, the difference in the amount of thermal conduction between the low- and high-speed rotary tumblers is still very clear (TDFs in Figure 4c–f), indicating the significant effect of duration time on thermal conduction in rotary tumblers.

Additionally, Figure 5c shows the evolution of mixing dimension at different rotation speeds (the insets), and the relation of developed mean mixing dimension (generally after $t=15$ s) to rotation speeds. It is seen from the insets of Figure 5c that the evolutions of mixing dimension in both time and revolutions are increasing until the developed states of mixing are established. Moreover, using a lower rotation speed to rotate the same revolutions (the top-right inset) can always lead to a larger mixing dimension, i.e., a more developed state of mixing, and vice versa. As aforementioned, it can be explained by the effect of TWW mechanism which depends mainly on time at this stage under the same revolution. In contrast, under the same time (the bottom-right inset), the TOW mechanism would dominate mixing. Thus, it is generally rapider to use a larger rotation speed to establish the developed mixing state. In addition, Figure 5c also indicates that a larger rotation speed can, in general, lead to a lower mean developed level of mixing. It is seen that the mean developed level of mixing is mainly determined by the rotation speed, i.e., the flow regimes, and, hence, independent of time and revolutions.

Probability density function of temperature discrepancy functions

Figures 3c–f and 4c–f visually show the distribution and differences of TDFs. Therefore, investigating the TDF characteristics quantitatively is necessary. Thus, the probability density function (PDF) of TDFs in Figures 6a and b corresponding to the "After the same evolution time" and "After the same revolution" sections, respectively, is explored. In general, PDF is formulated as the number of area cells $(\delta N(\Pi))$ with $\Pi \in [\Pi_0, \Pi_0+\delta\Pi]$ normalized by the total number of area cells $\left(N=\sum \delta N(\Pi)\right)$ covering all the heat-transfer interfaces, i.e.

$$p(\Pi)=\frac{\delta N(\Pi)}{N\delta\Pi}. \tag{17}$$

However, to incorporate the total amount of heat transfer interface, the current study used non-normalized PDF instead

$$p(\Pi)=\frac{\delta N(\Pi)}{\delta\Pi}. \tag{18}$$

By using non-normalized PDF, the area below $p(\Pi)$ indicates the absolute amount of heat transfer interface within $[\Pi, \Pi+\delta\Pi]$. In this way, the degree and amount of heat transfer under different conditions can be directly compared.

Figure 6a and b show the PDFs of TDF corresponding to "After the same evolution time" and "After the same revolution" sections, respectively. In Figure 6a, the PDF peak for TDF for $\omega=0.5$ (π/s) is approximately 27°C, whereas that for the others is roughly 35 to 37°C. The lesser temperature discrepancy for $\omega=0.5$ (π/s) than that for the others indicates a low degree of thermal conduction. Moreover, the peak values for $\omega=0.5$ (π/s) are significantly less than that for the others, indicating a significantly insufficient development of heat transfer. Recalling the fractal dimension of mixing interface in Figure 5a, the nearly consistent log(R)-log(s) for $\omega=1.0$–3.0 (π/s) leads to the nearly consistent PDFs of TDFs for $\omega=1.0$–3.0 (π/s). In other words, the degree of mixing of particles dominates the heat-transfer characteristics.

In Figure 6b, after the same revolution, the PDF peaks for high-rotation speed occur at low TDFs (ca. 15 to 20 °C), whereas those for low-rotation speed occur at high TDFs (ca. 30 to 40 °C). These results indicate that compared with low-rotation speed, high-rotation speed is relatively unfavorable for increasing TDFs with maximum probability because it is adverse to the thermal conduction of particles under the same revolution condition. This condition is caused by the decreased evolution time for the high rotation speed to reach the same revolution for larger TDF, as the more homogeneous temperature distribution has no sufficient time to develop. Moreover, the absolute PDF peaks at high-rotation speed are smaller than those are at low-rotation speed. This finding indicates that high rotation speed is unfavorable in increasing the PDF peaks because it is also adverse to thermal conduction development. This condition is caused by the relatively lower mixing level on the fine scales of the mixing interface compared with that of the low-rotation speed, in which the total "probability" for the thermal conduction is reduced. Thus, the two factors, mixing levels of the fine scale interface and temporal length, jointly contribute to thermal conduction development.

In addition, Figure 6c shows the temporal evolution of the mean TDFs over the tumbler. Under the same revolution, the TDF for low-rotation speed is larger than that for high rotation speed. The thermal conduction for low-rotation speed is more sufficiently developed than that for high-rotation speed. Thus, because of the common contribution of duration and fine mixing scale to the thermal conduction, using low-rotation speed is beneficial to heat transfer in tumblers. In conclusion, using low-rotation speed would be more favorable, provided the flow regimes are maintained (at least, the rolling regime), to enable sufficient heat transfer between particles, i.e., to obtain a homogeneous temperature distribution in the tumbler. It is based on the assumption that the total energy input for the rotating the tumbler should be

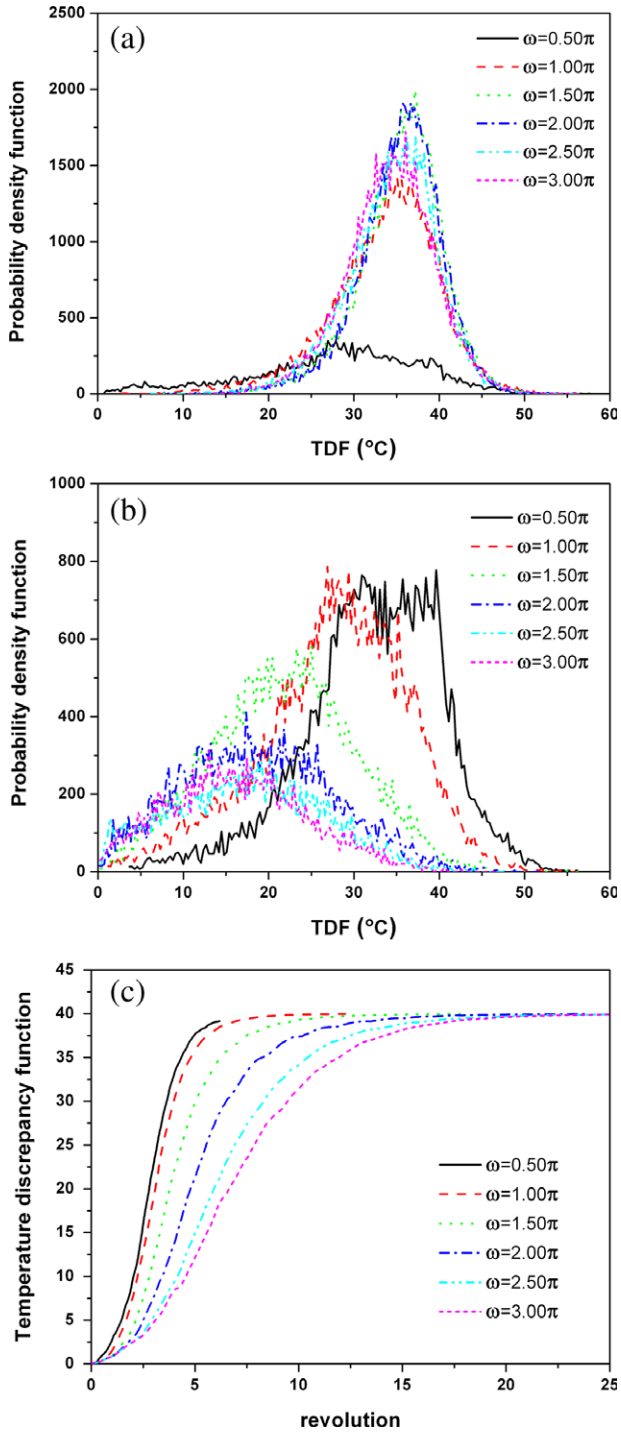

Figure 6. Probability density functions of TDF corresponding to Figure 3 (6a) and Figure 4 (6b), respectively.

[Color figure can be viewed in the online issue, which is available at wileyonlinelibrary.com.]

proportional to the number of revolutions so that the same revolution results in the same energy consumption.

Radial Distribution Function

Temperature-radial distribution function

In this section, the T-RDFs are used (Figure 7) for the macroscopic study of heat transfer. Figures 7b and c show the T-RDFs corresponding to the After the same evolution time and After the same revolution sections, respectively, and Figure 7a shows the initial T-RDF for all speeds.

Figure 7a indicates that the T-RDFs for all rotation speeds are the same because they evolved from the same initial state. However, after the same temporal evolution duration (Figure 7b), the T-RDFs change (1) The T-RDFs for the relatively high-rotation speed ω=1.0–3.0 (π/s) decrease

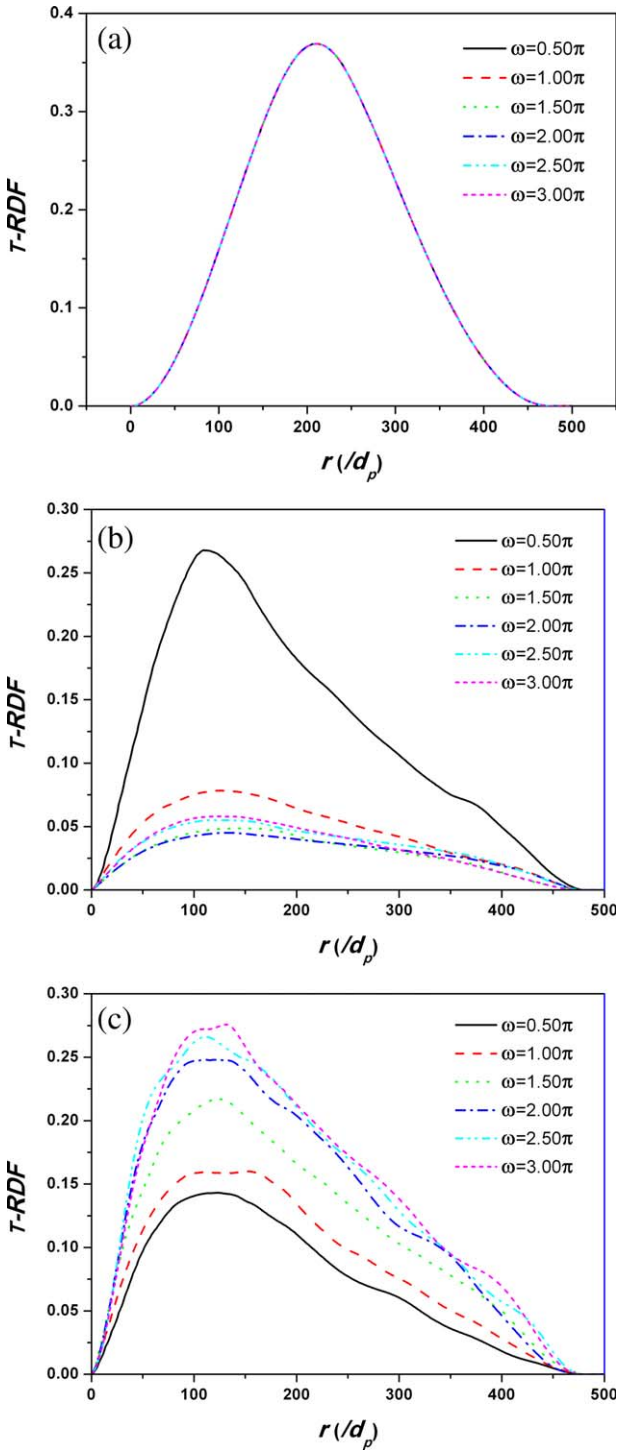

Figure 7. (a) Initial T-RDF for all speeds, (b) the T-RDFs at t=8.25 s, and (c) The T-RDFs after 2 revolution.

[Color figure can be viewed in the online issue, which is available at wileyonlinelibrary.com.]

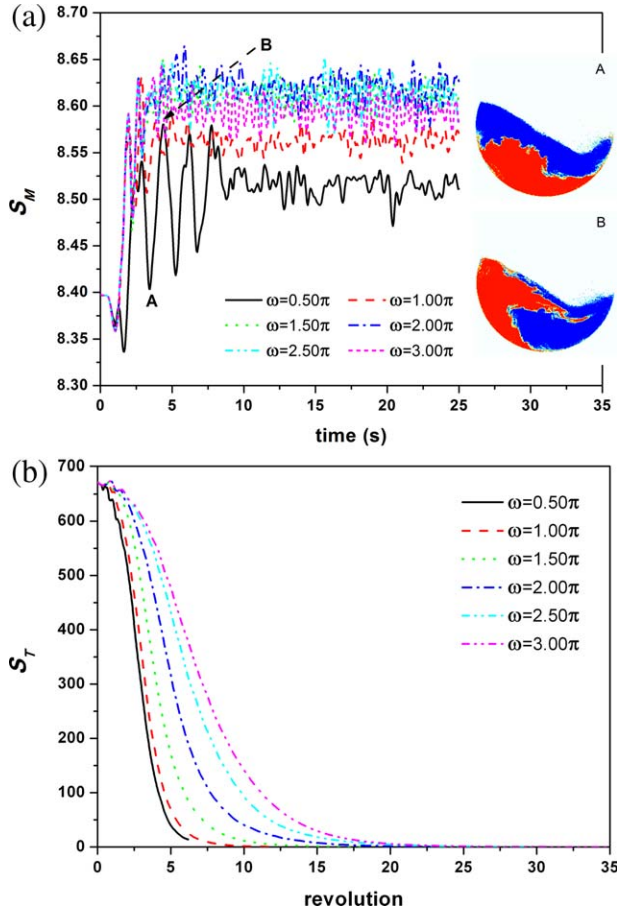

Figure 8. Information entropy for mixing S_M (a), and thermal conduction S_T (b).

The insets of Figure 8a show the corresponding distributions of particles at time points A and B, respectively. [Color figure can be viewed in the online issue, which is available at wileyonlinelibrary.com.]

throughout the whole range, indicating a decrease in temperature difference in the radial direction attributed to the mixing and thermal conduction between particles, (2) For low-speed ω=0.5 (π/s), the attenuation in the peak value is less than the former because of a lesser mixing degree effect, (3) The T-RDF peaks shift to a small radial distance from about r_p=200d_p to r_p=100d_p. The shift of the peaks is mainly caused by the evolution of particle mixing, as the dynamic mixing process changes the relative interdisplacements between the red (hot) and blue/green (cool) particle parts. Alternatively, the attenuation of T-RDF peaks is caused by the heat-transfer effect, as the relatively static thermal conduction leads to a reduction in temperature difference between the hot and cool particles.

Thus, under the same revolution condition (Figure 7c) the peak values of the T-RDFs decrease because of thermal conduction. Consequently, a higher speed corresponds to a small decrease in T-RDF because of the lesser temporal evolution duration than lower speed. Additionally, the shifts in T-RDF peaks are caused by the mixing evolution.

In summary, the change in T-RDF shows the different approaches of static thermal conduction and dynamic mixing, which jointly influence the heat-transfer characteristics of granular materials in a particular rotary system. The integration of these approaches is reflected in the following entropy analysis.

Entropy analysis

Based on Eqs. 14 and 15, information entropy or its analogical definition can be calculated as shown in Figure 8a and b. In mixing information entropy, generally, S_M increases with the increase in rotation speed (Figure 8a) and Table 2. That is, using a higher rotation speed can augment the degree of mixing in the tumbler, provided that the flow regimes in the tumbler are maintained. The slight decrease in the main mixing information entropy or mixing degree for ω=2.0–3.0 (π/s) is caused by the transition of the flow regime from cascading (Fr=1.16, where Fr=$\omega^2 R_0/g$ is the Froude number) to cataracting regimes (Fr=2.61). The pulsating variation of S_M in the early stage of Figure 8a is caused by the dissymmetrical distribution areas (Ω_a and Ω_b) of the hot and cool particles during the rotation of the tumbler. For example, The insets of Figure 8a shows the typical distributions corresponding to the locally lowest and highest points of S_M at t=3.45 and 4.35 s, respectively. It is seen that the former is an up-down distribution whereas the latter one is a left-right distribution, where the sizes of Ω_a and Ω_b for these two types of distribution are not the same. The rotation makes the variation of dissymmetry Ω_a and Ω_b periodically. However, the periodic fluctuations are rapidly attenuated as the mixing between the hot and cool particles advances.

Moreover, the information entropies corresponding to radial temperature discrepancies S_T decrease as the rotations increase (Figure 8b). The decrease in S_T is caused by the reduction of the temperature difference, as mixing evolves and subsequently causes reductions in T-RDF and S_T. More importantly, when the rotation speed increases, S_T decreases more slowly, indicating the less effective evolution of heat transfer among the granular materials with higher rotation speeds and validating the earlier analysis and conclusions on this issue.

Finally, the clear differentiation in S_T with different rotation speeds shows its feasibility through the good indication of heat-transfer evaluation. The duration time and mixing levels have been shown to contribute jointly to the thermal conduction characteristics. Evaluating the heat transfer efficiency of the tumbler under the sole contribution of particle mixing is now feasible by using information entropy based on the radial temperature discrepancy. If the information entropy increment $|\Delta S_T|$ is divided by the time duration $|\Delta\tau|$, the mean increase rate of information entropy is obtained as follows

$$|\dot{\bar{S}}_T| = \frac{|S_T(\tau_1) - S_T(\tau_0)|}{|\tau_1 - \tau_0|} = \frac{|\Delta S_T|}{|\Delta\tau|}, \quad \text{where } \tau_0 = 0 \text{ here.} \tag{19}$$

Equation 19 may indicate the mean efficiency of heat transfer arising from the sole mixing effect. Figure 9 shows

Table 2. Mean Information Entropies for Various Rotation Speeds after t=2.5 s

Rotating speed ω (rad/s)	Froude number Fr=$\omega^2 R/g$	Flow regime	Mean information entropy (dB)
0.5π	7.25 × 10^{-2}	Rolling	8.513
1.0π	0.290	Rolling/Cascading	8.563
1.5π	0.653	Rolling/Cascading	8.611
2.0π	1.160	Cascading/ Cataracting	8.618
2.5π	1.813	Cataracting	8.612
3.0π	2.610	Cataracting	8.595

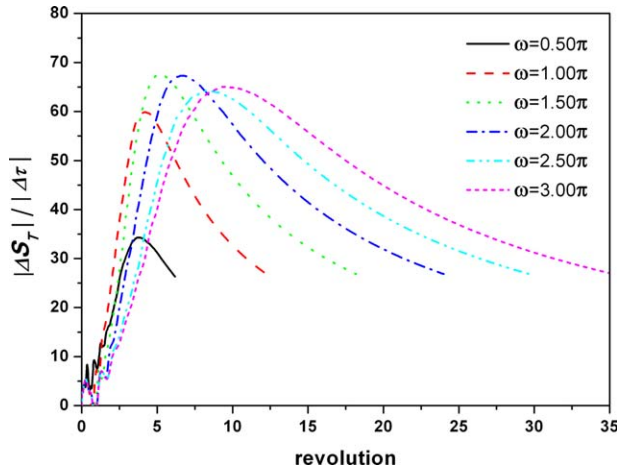

Figure 9. Mean increase rate of temperature information entropy.

[Color figure can be viewed in the online issue, which is available at wileyonlinelibrary.com.]

that the maximum increase rate of information entropy for each rotation speed exists, indicating that the maximum operating condition has the best efficiency. For example, for ω=1.0 (π/s), the maximum increase rate occurs at about five revolutions, after which the heat-transfer efficiency cannot be maintained to be as high as before by the rotation because the temperature discrepancy is very small (Figure 8b). Moreover, for different rotation speeds, the maximum increase rate occurs at different revolutions. The larger the rotation speed is, the larger the critical point of revolution for maximum increase rate. Before the critical point is reached, low rotation speeds (except ω=0.5 π/s for the pure rolling regime) always produce higher heat-transfer efficiency. The opposite is true after the critical point is reached.

Figure 9 can be regarded as a performance plot for the tumbler. It not only shows the evaluation of heat transfer levels, increase rates, and transition points with maximum efficiency, but also provides clearly the method for determining the most effective operating conditions for the tumbler. For example, for using a constant rotation velocity, it is best to use ω=1.0 π/s for less than three revolutions; but to use ω=3.0 π/s for more than 10 revolutions. Moreover, considering the envelope of the curves, the best efficient way is to use ω=1.0 π/s before three revolutions and transit to use ω=1.5 π/s until 5 revolutions, and then go on transiting to ω=2.0, 2.5, 3.0π/s, etc. In other words, this enveloping approach has the highest mean increase rate of entropy S_T, or the best efficient heat conduction, provided the flow regimes remain valid for mixing and conduction.

Conclusion

This study investigated the mixing and thermal conduction of granular particles in tumblers using DEM and incorporated thermal conduction between contact particles. The mixing and WT structures, as well as the temperature discrepancy from the ideal adiabatic case without heat transfer, are shown after the same time evolution and revolution through appropriately defined evaluation functions. The results are summarized briefly as follows:

1. After the same temporal evolution, the mixing degree generally increases as the rotation speed increases from the rolling regime of ω=0.5 (π/s) to the rolling/cascading regime of ω=1.0–2.0 (π/s). However, in the cataracting flow regime with a very large rotation speed of ω=2.5–3.0 (π/s), the mixing degrees are less than those of the rolling/cascading regime. However, under the same revolution, the large-scale structure of the mixing interface remains the same for different speeds, whereas the fine-scale mixing interface increases as the rotation speed decreases because of the increase in duration time for the evolution of fine mixing structures.
2. The PDF of TDF explains the joint contribution of mixing degree and duration time to the granular heat transfer, i.e., the longer duration time and finer mixing structures at a lower rotation speed enlarge the regions of greater TDFs, or higher developed degrees of heat conduction.
3. The change in T-RDF shows the different approaches of static thermal conduction and dynamic mixing, which jointly contribute to the heat-transfer characteristics, including the peak shift of T-RDF attributed to the evolution of mixing and the attenuation of T-RDF due to the duration of the thermal conduction.
4. The entropy analysis shows the integration effect of the two contributory approaches. Dividing the temperature information entropy by the duration time provides a good method for determining the average efficiency of the tumbler under various operating conditions and for finding the most effective operating condition for heat transfer in the tumbler.

Acknowledgments

The authors are grateful for the support of this research by the National Natural Science Foundation of China (Grant No. 51106180) and the research funds of China University of Petroleum, Beijing (No. BJ-2010-03).

Notation

Scalars

Bi = Biot number
c_p = particle specific heat
d_p = particle diameter
D_β = fractal dimension of the interface
E = restitution coefficient
f_{ab} = radial distribution function
g_{ab} = temperature radial distribution function, T-RDF
Fr = Froude number
I_p = moment of inertia of particle
K = stiffness factor
k_n = normal stiffness factor
m_p = particle mass
n_a, n_b = number concentration of the red and blue particle, respectively.
N = number of cells
p = probability density function
q_c = heat transfer rate per unit temperature difference
Q_{ij} = total rate of heat transfer
r = radial distance
r_p = particle radius
r_c = contact radius
$R(s)$ = length of mixing interface
s = scale of the covering boxes
S_M, S_T = shannon information entropy for mixing and heat transfer, respectively
T_i, $T_j$$T_a$, T_b = particle temperature
α = thermal diffusivity

β = damping coefficient
γ = friction coefficient
λ_p, λ_f = thermal conductivity of particle and air, respectively
ω = rotation speed of the tumbler
$\Re$ = dimensionless function for evaluation of mixing degree
Θ = weighted temperature (WT)
Π = temperature discrepancy function (TDF)
Ω_a, Ω_b = area of regions occupied by the "*a*" and "*b*" particle, respectively

Vectors

$\boldsymbol{\omega_p}$ = particle angular velocity
$\boldsymbol{x}$ = particle position vector
$\boldsymbol{f_c}$ = particle–particle contact force
$\boldsymbol{F}$ = particle total force
$\boldsymbol{g}$ = gravity acceleration
$\boldsymbol{T_p}$ = torque
$\boldsymbol{n}$, $\boldsymbol{t}$ = normal and tangential vectors, respectively

Literature Cited

1. Boateng AA. Rotary Kilns: Transport Phenomena and Transport Processes. Burlington, MA: Butterworth-Heinemann; 2008:1:1–14.
2. McCarthy JJ, Shinbrot T, Metcalfe G, Wolf JE, Ottino JM. Mixing of granular materials in slowly rotated containers. *AIChE J*. 1996;42:3351–3363.
3. Cisar SE, Ottino JM, Lueptow RM. Geometric effects of mixing in 2D granular tumblers using discrete models. *AIChE J*. 2007;53:1151–1158.
4. Meier SW, Lueptow RM, Ottino JM. A dynamical systems approach to mixing and segregation of granular materials in tumblers. *Adv Phys*. 2007;56:757–827.
5. Mellmann J, Specht E, Liu X. Prediction of rolling bed motion in rotating cylinders. *AIChE J*. 2004;50:2783–2793.
6. McCoy BJ, Madras G. Cluster kinetics of granular mixing. *AIChE J*. 2005;51:406–414.
7. Mellmann J. The transverse motion of solids in rotating cylinders-forms of motion and transition behavior. *Powder Technol*. 2001;118:251–270.
8. Wightman C, Moakher M, Muzzio FJ. Simulation of flow and mixing of particles in a rotating and rocking cylinder. *AIChE J*. 1998;44:1266–1276.
9. Portillo PM, Muzzio FJ, Ierapetritou MG. Hybrid DEM-compartment modeling approach for granular mixing. *AIChE J*. 2007;53:119–128.
10. Vargas WL, Hajra SK, Shi D, McCarthy JJ. Suppressing the segregation of granular mixtures in rotating tumblers. *AIChE J*. 2008;54:3124–3132.
11. Geng F, Yuan Z, Yan Y, Luo D, Wang H, Li B, Xu D. Numerical simulation on mixing kinetics of slender particles in a rotary dryer. *Powder Technol*. 2009;193:50–58.
12. Cleary PW, Sinnott MD. Assessing mixing characteristics of particle-mixing and granulation devices. *Particuology*. 2008;6:419–444.
13. Woodle GR, Munro JM. Particle motion and mixing in a rotary kiln. *Powder Technol*. 1993;6:241–245.
14. Parker DJ, Dijkstra AE, Martin TW, Seville JPK. Positron emission particle tracking studies of spherical particle motion in rotating drum. *Chem Eng Sci*. 1997;52:2011–2022.
15. Yamane K, Nakagawa M, Altobelli SA, Tanaka T, Tsuji Y. steady particulate flows in a horizontal rotating cylinder. *Phys Fluids*. 1998;10:1419–1427.
16. van Puyvelde DR, Young BR, Wilson MA, Schmidt SJ. Experimental determination of transverse mixing kinetics in a rolling drum by image analysis. *Powder Technol*. 1999;106:183–191.
17. Metcalfe G, Shinbrot T, McCarthy JJ, Ottino JM. Avalanche mixing of granular solids. *Nature*. 1995; 374:39–41.
18. Kwapinska M, Saage G, Tsotsas E. Mixing of particles in rotary drums: A comparison of discrete element simulations with experimental results and penetration models for thermal processes. *Powder Technol*. 2006;161:69–78.
19. Kwapinska M, Saage G., Tsotsas E. Continuous versus discrete modeling of heat transfer to agitated beds. *Powder Technol*. 2008;181:331–342.
20. Shi D, Vargas WL, McCarthy JJ. Heat transfer in rotary kilns with interstitial gases. *Chem Eng Sci*. 2008;63:4506–4516.
21. Figueroa I, Vargas WL, McCarthy JJ. Mixing and heat conduction in rotating tumblers. *Chem Eng Sci*. 2010;65:1045–1054.
22. Hillborn RC. Chaos and Nonlinear Dynamics. New York, NY: Oxford University Press; 1994.
23. Cho YJ, Kim SJ, Nam SH, Kang Y, Kim SD. Heat transfer and bubble properties in three-phase circulating fluidized beds. *Chem Eng Sci*. 2001;56:6107–6115.
24. Zhong W, Zhang M. Characterization of dynamic behavior of a spout-fluid bed with Shannon entropy analysis. *Powder Technol*. 2005;159:121–126.
25. Cundall PA, Strack ODL. A discrete numerical model for granular assemblies. *Geotechnique*. 1979;29:47–65.
26. Argo WB, Smith JM. Heat transfer in packed beds: prediction of radial rate in gas-solid beds. *Chem Eng Prog*. 1953;49:443–451.
27. Batchelor GK, O'Brien RW. Thermal or electrical conduction through a granular material. *Proc R Soc Lond*. 1977;355:313.
28. Vargas WL, McCarthy JJ. Heat conduction in granular materials. *AIChE J*. 2001;47:1052–1059.
29. Arntz MMHD, den Otter WK, Briels WJ, Bussmann PJT, Beeftink HH, Boom RM. Granular mixing and segregation in a horizontal rotating drum: A simulation study on the impact of rotational speed and fill level. *AIChE J*. 2008;54:3133–3146.
30. Gui N, Fan JR, Cen KF. A macroscopic and microscopic study of particle mixing in a rotating tumbler. *Chem Eng Sci*. 2010;65:3034–3041.

Manuscript received Dec. 21, 2011, revision received Aug. 7, 2012, and final revision received Dec. 7, 2012.